Coupled deep mantle carbon-water cycle: Evidence from lower mantle diamonds

W. Wang^{1†}, O. Tschauner², S. Huang², Z. Wu¹, Y. Meng³, H. Bechtel⁴, H.-k. Mao³
Affiliations:

¹Laboratory of Seismology and Physics of Earth's Interior, School of Earth and Space Sciences, University of Science and Technology of China, Hefei, China.

²Department of Geoscience, University of Nevada Las Vegas, Las Vegas, Nevada 89154, USA.

³Center for High Pressure Science and Technology Advanced Research, Shanghai 201203, China

⁴Advanced Light Source, Lawrence Berkeley Nat. Lab.

[†]Now at Department of Earth Sciences, University College London, London WC1E 6BT, United Kingdom

Correspondence: wz30304@mail.ustc.edu.cn

Abstract

1

2

3

4

5

6

7

8

Diamonds form in a variety of environments between subducted crust, lithospheric and deep mantle. Recently, deep source diamonds with inclusions of the high-pressure $\rm H_2O$ -phase ice-VII were discovered. These deep sourced diamonds link the global carbon- and water-cycle. We assess quantitatively the pressures and temperatures of entrapment of $\rm H_2O$. We show that the diamonds from the deepest source form at depths down to ~ 800 +/- 60 km but 400 K below average mantle temperature. Such wet cool environments could be produced by the decomposition of dense hydrous mantle silicate.

9

10

11

12

13

14

15

16

17

18

19

20

21

22

23

24

25

26

27

28

Introduction

Decades of effort in geodynamic modeling and seismic observations have confirmed the presence of lateral heterogeneities in the transition zone (TZ) and lower mantle (LM) of Earth. These heterogeneities are distinguished through reduced seismic velocities and seismic wave reflections. Presence of melt or fluid, thermal and chemical variations in the mantle can cause reduction of seismic velocities. In this context diamonds provide key information because they are part of the global deep carbon cycle and, in some cases, contain inclusions which were entrapped in the TZ or LM ¹⁻⁶. Such diamonds are proposed to form from reduction of carbonaceous fluids or melts infiltrating the deep mantle ⁷. Recently, the discovery of hydrous ringwoodite ³ and ice-VII ⁵ as inclusions in diamonds correlates the question of water storage in the deep mantle with the carbon-cycle. It was also shown that some inclusions in diamonds sustain remnant pressures of several gigapascals (GPa) 4,5, high enough to imply formation in the TZ or LM. Hence, these inclusions provide the only direct mineralogical information about the TZ and LM whereas products of retrograde transformations of high-pressure minerals ^{1,2} conserve composition but no quantifiable information about the P-T of their entrapment. Here we show that inclusions with high remnant pressure not only represent entrapment in environments rich in carbonaceous aqueous fluid, which permit formation of diamond ⁷ and ice-VII ⁵, but that they

generally represent very cool environments within the lower mantle, above the solidus of wet carbonated but below the solidus of wet peridotite. In particular, we determine the actual depth and temperature of these environments.

Our approach is based on the *in-situ* observation of µm- to sub -µm-scale mineral inclusions in diamonds which bear remnant pressures in the range of 2 to 14 GPa (Fig. 1). These remnant pressures define foot points of their pressure-temperature (P-T) paths which these inclusions experienced between the time of their entrapment in growing diamond and presence ^{4,5}. Inclusions that were entrapped at the same depth in the Earth have P-T paths which intersect at the same P-T point. Here we use a new concept of correlating P-T paths of different inclusions in one diamond for assessing the P-T of entrapment (see Methods). This is different from earlier assessments which involve a priori assumption about the geotherm ^{4,8}. At the same time, we take full account of viscoelastic relaxation of host diamond (Methods). In our approach assessment of the P-T paths is in two steps: First through the condition of equal strain of host diamond and inclusions (isomeke ⁹, which we call here elastic paths to emphasize the abstraction from viscoelastic relaxation) and, second, the role of viscoelastic relaxation of diamond ^{10,11}. Finally, we show that accounting for viscoelastic relaxation gives temperatures which match those obtained from nitrogen defects in diamond ¹². In our approach P and T are strictly correlated. Thus, independent confirmation of T also confirms that the assessment of P is correct.

49

50

51

52

53

54

55

56

29

30

31

32

33

34

35

36

37

38

39

40

41

42

43

44

45

46

47

48

Results

The information of diamonds investigated in this work is described in detail in Methods. We conducted X-ray diffraction measurements on the inclusions. The diffraction- and X-ray fluorescence data of ilmenite (ilm90) and taenite (Fe50Ni50) from Diamantina-1 gave following volumes: 307.9(5) and 44.9(3) Å³, respectively. The diffraction data of the Orapa samples had been reported previously (see online depository of Tschauner et al. (2018) ⁵). We determined Infrared spectra of diamonds

and used the calibrations by Boyd et al. ^{13,14} for estimating the amount of nitrogen in A- and B-type defects, respectively. The amount of D-type defects was found to be less than 10 ppm in any specimen based on the calibration by Clark and Davey ¹⁵, and was neglected as being within uncertainties of the amounts of A- and B-defects. Nitrogen contents and estimated mantle residence temperatures are presented in table 1. The nitrogen contents from A- and B-type defects range from 52 to 96 ppm and from 49 to 134 ppm, respectively. The corresponding percentage of A-defects, and the approximate age of the diamonds (Table 1) were used to estimate average mantle residence temperatures ^{16,17}. The fitted defect profiles and observed spectra are shown in Fig. S1.

Remnant 300 K pressures of inclusions were assessed from their unit cell volumes corrected for the elastic relaxation of diamond at 300 K ⁹. The corrected pressures were used as foot points for calculations of pressure-temperature (P-T) paths for the inclusions and the paths were calculated based on the condition of equilibrated strain of inclusion and diamond ("elastic path"). In a second step the paths were corrected for viscoelastic relaxation of the hosting diamond.

Discussion

We start with discussing the common case of annealed inclusion-diamond systems. Temperatures near the average mantle adiabat ¹⁸ are well above the temperatures of viscoelastic relaxation of diamond ^{10,11}. We expect that over time stresses between inclusions and host diamond relax. Their pressure and temperature (P-T) equilibrate with the surrounding mantle and follow a more or less adiabatic path upon ascent until temperature drops below the brittle- to viscous transition in diamond. This is illustrated in Fig. 1a for inclusions in a type IaB diamond from the Diamantina alluvial deposits. The remnant pressures of the inclusions are 1 and 4 GPa, respectively, at 300 K, which are remnant pressures values typically found for Brazilian super-deep diamonds at least formed within the TZ ¹⁹. They start intersecting right at the

viscoelastic limit of diamond of 1200-1300 K ^{10,11} above 9.8 GPa. Any memory of the P-T path above that limit is lost although we can use the percentage of remnant A-type defects in this diamond to assess temperature ¹² and the elastic P-T path to estimate a minimum P of entrapment (Fig. 1a and Table 1), which is consistent with the Ni-content of the taenite inclusions of this diamond ²⁰. We expect to find this convergence of the elastic P-T paths at the elastic-viscoelastic transition of diamond for deep mantle inclusions in general. In fact, diamonds from Juina and Kankan which originated in the deep mantle contain inclusions which formed retrogradely from higher pressure minerals ^{1,2} or high pressure minerals relaxed to low remnant pressure ³, in accordance with viscoelastic relaxation over extended geologic time at a depth shallower than the depth of entrapment. This long relaxation time is also reflected in the extended annealing of nitrogen defects to virtually only type B ⁴ or N-free type II diamonds ^{1,2}.

However, it comes as a surprise that some diamonds from the deep mantle contain inclusions whose elastic release P-T paths do not intersect at the elastic-to-viscoelastic transition in diamond but at noticeably higher pressure and temperature (Fig. 1b). A similar finding was reported by Anzolini et al. (2019) for single periclase inclusions from the TZ ¹⁹. These sustained pressure differences within the viscoelastic regime clearly show that these inclusions did not experience full relaxation in viscoelastically deforming diamond upon ascent and that they conserve an at least partial record of their actual P-T conditions of entrapment in the deep mantle. More precisely, these diamonds have ascended at rates higher than complete viscoelastic relaxation of their host diamonds. One may argue that such intersection at high P-T could be incidental. However, the elastic P-T paths of inclusions in diamond are quite steep (Fig. 1). Hence, their intersection at a pressure within mantle P-T mathematically implies that their entrapments has occurred within a limited pressure range in the mantle: elastic P-T paths of inclusions of clearly different origin (such as lithospheric inclusions in fibrous rims or along cracks compared to inclusions in the kernel of these diamonds) do not intersect at a positive temperature or within any plausible P-T bounds.

We can use the sustained pressure differences of high-pressure inclusions to constrain the actual P-T conditions of entrapment. We examine two limiting cases: 1) Intersection of the elastic P-T paths, 2) convergence along an adiabatic path based on the observed excess pressure at the diamond viscoelastic limit (Fig. 1b, further details in Methods). As a check, we determine T independently through the N-aggregation state in the diamonds ¹². We find that the adiabatic path gives the same temperatures as the N-aggregation in their host diamonds within uncertainties (Table 1 and Fig. 2). Therefore, the adiabatic path provides realistic temperature estimates for the inclusions. In turn, the elastic paths markedly overestimate T and underestimate P. Along an adiabatic path P and T are correlated. Therefore, with T independently confirmed, our approach also provides reliable estimates of P.

The results are summarized in Fig. 2. All P-T points are above the solidus of wet carbonated peridotite ²¹. All diamonds with ice-VII inclusions fall within a P-T range between the solidus of wet and the wet carbonated peridotite 21 but quite below the solidus of dry carbonated 7 even alkaline rich peridotite 22 . Below ~ 800 km depth the P-T points of entrapment are at the decomposition line of the dense hydrous magnesium silicate phase D ²³. In other words, the formation of the deepest know diamonds and H₂O-inclusions match the decomposition of hydrated mantle silicate. In sum, formation of H₂O-bearing sublithospheric diamonds is tied to wet cool environments at depths down to 820 km, 200-500 K below a reference average mantle adiabat 18. Hence, we have identified the depth-temperature regime for diamonds from ultradeep sources within narrow bounds and to within the LM. This holds at least for diamonds with inclusions at high remnant pressures. For other deep source diamonds, residence at shallower depth at temperatures above the elastic-viscoelastic limit of diamond has removed the record of their origin beyond the observation of transformation products of former high pressure phases. However, the observation of hydrous minerals ^{3,24,25} and of taenite and iron as inclusions in ultradeep source diamonds ^{3,5,26} point toward a common origin through different paths and timescales of ascent. Overall, deep source

diamonds form between 500 and 860 km depth. Within this context we locate diamond formation in the LM at 800±60 km and 370-560 K below the average mantle at that depth consistent with dehydration of phases B and D ²³ (Fig. 2). Remnant water may be kept to even greater depth ²³ but 800±60 km defines the deepest part of the mantle that is still involved in recycling water and carbon as witnessed through diamond, based on our data. Hence, we establish a conjunction between these conditions within the LM, the deep carbon- and the deep water cycle.

Conclusion

We established an independent and quantitative assessment of pressure and temperature of formation of diamonds. The approach is based on the *in-situ* observation of μ m- to sub - μ m-scale mineral inclusions in diamonds which bear remnant pressures in the range of 2 to 14 GPa. These remnant pressures define foot points of their P-T paths which these inclusions experienced between the time of their entrapment in growing diamond and presence. We assessed the P-T paths in two steps: First through the condition of equal strain of host diamond and inclusions and, second, the role of viscoelastic relaxation of diamond. The results show that deep sourced diamonds form at ~ 800 km depth but 400 K below average mantle temperature. Such cool environments rich in carbonaceous aqueous fluid, which is above the solidus of wet carbonated but below the solidus of wet peridotite, permit formation of diamond and ice-VII.

Materials and Methods

Description of the diamonds

GRR1507 is a type IaAB diamond (Fig. S1). The sample was a polished 200 μ m thick wafer that was cut along 001 out of an octahedral crystal of 85.6 mg weight. The crystal had a greenish outer rim and a clear kernel. The rim is rich in inclusions of remnant pressure of less than 1 GPa to nearly ambient (calcite, chromite) and exhibits

significantly higher percentage of A-type N-defects than the kernel. Fig. S1a shows a representative IR-spectrum from the kernel of this diamond. Micro-X-ray fluorescence maps of the kernel region exhibit two concentric zones of octahedral habit marked by a boundary rim of elevated impurity level but themselves not distinguished in traceelements or impurities. The innermost zone exhibits few, isolated inclusions (iron, ilmenite, ice-VII, Table 1). A healed crack propagates from the rim into the outer zone of the kernel and contains low-pressure inclusions (calcite, sellaite, a fluid methanerich species, olivine Fo96-97, enstatite). No differences in N-aggregation state is resolved for the two zones of the kernel. However, we note that both zones are sampled by the IR beam in transmission. GRR1519 is a hexahedral crystal of pale green color from Orapa, with frosted faces and few channels. The original weight was 7.7 mg. We examined a piece laser-cut and polished along 100. M57666 is a clear piece of an originally 49.8 mg macle from Orapa that was mechanically crushed from GRR1521 Inclusions of ice-VII and taenite occur in M57666. Diamantina-1 is an 80-µm thick wafer laser cut from a clear, rounded dodecahedral crystal with trigons of originally 16mg weight from the Diamantina alluvial deposits.

X-ray diffraction and X-ray fluorescence analysis

X-ray diffraction data were collected at beamlines 13-IDB,-IDE, and 34-IDE at energies of 30, 19, and 22 keV, respectively. The primary beams were focused by elliptical mirrors to micrometer-scale (34-IDE: 0.5 micrometer) beam diameters. Diffraction data were collected with area detectors, calibrated and integrated with Dioptas. X-ray fluorescence was excited by the same primary beams and collected with a Vortex detector. The diffraction data of the Orapa samples had been reported previously (see online depository of Tschauner et al. (2018) ⁵). The diffraction- and X-ray fluorescence data of ilmenite (ilm90) and taenite (Fe50Ni50) from Diamantinas-1 gave following volumes: 307.9(5) and 44.9(3) Å³.

Infrared spectra of the examined diamonds

The spectra of all samples except GRR 1521 were collected in transmission at beamline 1.4, ALS, with a Nicolet Magna 760 FTIR bench and a Nic-Plan IR microscope with a 32x magnification Schwarzschild objective, with 1 cm⁻¹ resolution and a HgCdTe detector with a KBr beam splitter. Apertures were set to 20x20 to 40×60 um² spatial resolution. The spectrum of the sample Diamantina-1 was obtained from the uncut specimen. The spectrum of GRr1521 was taken from a crushed, clear piece with a Thermo-Nicolet iS50 FTIR at the mineral spectroscopy laboratory at Caltech in transmission with a glow bar source and 2 cm⁻¹ resolution. All other spectra were obtained from laser-cut, polished platelets. A synthetic type II diamond was used for assessing absorbance between 1000 and 1500 cm-1. Spectra were background subtracted and scaled to an equal thickness of 10 mm. Contribution of A-, B-, and Dtype defect bands were assessed by using the pure defect type spectra reported by Taylor et al. (1990) ¹². We used the calibrations by Boyd et al. ^{13,14} for estimating the amount of nitrogen in A- and B-type defects, respectively. The amount of D-type defects was found to be less than 10 ppm in any specimen based on the calibration by Clark and Davey 15 and was neglected as being within uncertainties of the amounts of A- and B-defects. The nitrogen contents from A- and B-type defects, the corresponding percentage of A-defects and the approximate age of the diamonds (table 1) were used to estimate average mantle residence temperatures ^{16,17}. The fitted defect profiles and observed spectra are shown in Fig. S1. These spectra and fits correspond to the results in Table 1.

219

220

221

222

223

197

198

199

200

201

202

203

204

205

206

207

208

209

210

211

212

213

214

215

216

217

218

Ab inito calculations

Computational calculations were conducted using the Quantum Espresso package ²⁷ (ilmenite and liuite ²⁸), Vienna ab initio simulation package (VASP) ²⁹ plus finite displacement approach ³⁰ for ice-VII, first-principles molecular dynamics simulations

(FPMD) on the cubic box containing 210 H₂O molecules for fluid H₂O, and equation of state of iron phases from Dorogokupets et al. (2017) ³¹.

224

225

226

227

228

229

230

231

232

233

234

235

236

237

238

239

240

241

242

243

244

245

246

247

248

249

250

251

For ilmenite and liuite the local density approximation (LDA) was used for assessing the exchange correlation. The energy cutoff for electronic wave functions was set at 70 Ry. The oxygen pseudopotential was generated using the Troullier-Martins method ³² with a cutoff radius of 1.45 Bohr and a valence configuration of 2s²2p⁴. The pseudopotentials for iron (Fe) and titanium (Ti) were generated using the Vanderbilt method ³³ with a valence configuration of 3s²3p⁶3d^{6.5}4s¹4p⁰ for iron and a valence configuration $3s^23p^63d^24s^2$ for titanium. The cutoff radii for both pseudopotentials are 1.8 Bohr. Due to the existence of large on-site Coulomb interactions among the localized electrons (e.g., 3d electrons) ³⁴, we introduced a Hubbard U correction to the LDA (LDA+U). Hubbard U values for Fe and Ti atoms in ilmenite were nonempirically determined using linear response method ³⁵. Crystal structures of ilmenite were well optimized using the damped variable cell shape molecular dynamics at variable pressures on a 6×6×6 k-point mesh, and vibrational density of state (VDoS) were calculated using the finite displacement method ³⁰. However, the vibrational phonon calculations for liuite report some imaginary frequencies, which hampers the calculations of high-temperature equation of state (EoS). Here we obtained the 0 K isotherm of luite from LDA+U calculations and estimated the EoS at different temperatures using the thermal expansion of bridgmanite ³⁶. We assumed that temperature shows a similar effect on the volume changes of FeTiO₃ and MgSiO₃ perovskites.

Due to the failure of LDA in predicting the properties of H₂O system ³⁷, we performed first-principles calculations for ice-VII and H₂O fluids by adopting the generalized gradient approximation (GGA) ³⁸ for the exchange correlation function. All calculations for ice-VII were done using VASP code ²⁹ and the PBE-type of pseudopotentials for hydrogen and oxygen were used. The energy cutoff for plane waves was set as 700 eV. For solid ice-VII, relaxed crystal structures under different

pressures were obtained by optimizing cell parameters and atomic coordinates at an $8\times8\times8$ k-point mesh grid and their VDoS were derived from the finite displacement method 30 . For H_2O fluids, we conducted FPMD simulations on the cubic box containing 210 H_2O molecules to determine the EoS. FPMD simulations were propagated in the canonical ensemble (NVT) with the Nose thermostat and the Brillouin zone was sampled at gamma point. All simulations on cubic boxes with variable volumes lasted at least 40000 steps with a time step of 1.0 fs, and temperature was set as 600 K, 900 K, 1200 K, 1500 K, 2000 K, 2300 K, 2500 K, 2700 K, and 3000 K. Pressures at different temperatures and volumes can be derived by calculating ensemble averages of the instantaneous pressure after reaching the equilibrium state.

All calculations were checked against available experimental results ^{39,40,49–57,41–48}. Predicted volumes of ice-VII at 300 K agree well with experimental measurements with largest discrepancy < 1% up to 25 GPa (Fig. S3). The density of H₂O fluid at high P-T conditions are compared with available experimental data ^{49–51} with discrepancy of less than 2%. The density of H₂O fluid nonlinearly depends on pressure; at 1500 K, the pressure derivative of density decreases from 0.043 g/(cm³•GPa) at 10 GPa to 0.019 g/(cm³•GPa) at 30 GPa. The temperature effect on H₂O density is almost linear and similar at different pressures. For instance, at 20 GPa, the H₂O density decreases by ~ 3.0% when temperature increases from 1500 K to 2000 K. For ilmenite, we calculated the EoS of the FeTiO₃ end-members but used the empirical volumes of the observed ilmenite-geikielite solid solutions. Thereby we avoid the issue of modeling the real solid solution over the entire range but we assume the mixing volume does not change with temperature. For ilmenite discrepancies between calculated and observed volumes are within the experimental range of 1.5% ^{52–54}. In addition, the predicted volumes of liuite also agree well with experimental data ^{56,57}.

Determination of P-T paths

Remnant 300 K pressures of inclusions were assessed by synchrotron microdiffraction of their unit cell volumes at beamlines 13-IDDIDE, and 34-IDD. Experimental parameters and data are provided in the Supplement. We used empirical equations of state of the mineral inclusions for the given composition. Subsequently, the elastic relaxation of diamond at 300 K was corrected 9. The corrected pressures were used as foot points for calculations of pressure-temperature (P-T) paths for the inclusions and the paths were calculated based on the condition of equilibrated strain of inclusion and diamond ('elastic path'). We used the variance of pressures for separate inclusions of the same phase as upper and lower bounds for the foot points. Because of the low compressibility, low thermoelastic softening, and low thermal expansivity of diamond, the elastic paths are close to isochores ^{4,5}. First order phase transitions were addressed by calculating separate paths for low- and high P-T phases, assessment of the pressure difference at the phase boundaries (coexistence range) and subsequent correction for diamond relaxation under isothermal conditions. The required thermoelastic parameters were obtained from *ab initio* calculations and literature data. Details of these calculations and the correction for minor chemical components are described above. By using empirical foot pressures we largely circumnavigate the issue of possible over- or underestimation of computed volumes from insufficient correction of electron exchange correlation. Consequently, deviations between computed and available empirical high P-T volume data are within the uncertainties of the latter. Generally, we used these deviations and the uncertainties of the foot point pressures in combination to estimate upper and lower bounds of P-T paths (Fig. 1). Uncertainties of intersection points are defined by the upper and lower intersection points of intersecting paths in P-T space.

279

280

281

282

283

284

285

286

287

288

289

290

291

292

293

294

295

296

297

298

299

300

301

302

303

304

305

306

All data are given in Table 1, Table S1-S3, and are plotted in Fig. 1 and Fig. S2. Partial relaxation is a time-dependent, therefore, path-dependent process. Thus, change of pressure, volume, and temperature are path-dependent as well. In addition, partial relaxation is expected to differ for different inclusions, depending on their elastic

moduli, phase transformations, and their actual sizes and shapes. We constrain this unknown time-dependent P-T path by two non path-dependent limiting cases (Fig. 1b). In case I, the intersection of the elastic P-T paths defines the upper limit of temperature and the lower limit of pressure of their entrapment P-T point because it defines the most rigid response of diamond to the stress excerted by the inclusions at a given P-T of the surrounding rock. This is shown in Fig. 1b. For all examined specimens these P-T intersection points are well above the viscoelastic limit of diamond and well above the present mantle geotherm (Fig. 1b). In case II we look at the pressure differences between these inclusions at the elastic-viscoelastic transition temperature and use an adiabatic path for assessing the P-T of entrapment as a lower T-limit (Fig. 1b). It turns out that within uncertainties the adiabatic P-T paths gives the same temperature as the correlation of nitrogen content in the host diamonds with percentage of A-type defects (Table 1 and Fig. 2). As a low temperature limit we assume that an adiabatic path intersects the viscoelastic limit temperature of 1200-1300 K at the lowest observed pressure of the inclusions (Fig. 1b). In case of complete relaxation the inclusions would have the same pressure at this temperature. The observed ΔP at the diamond elasticviscoelastic transition quantifies an excess pressure and a corresponding adiabatic ΔT (Fig. 1b). The transition from brittle elastic to visco-elastic behavior of diamond has been aexamined for single and poly-crystals (10, 11), the latter giving lower bounds. Without discussing these differences, the possible effect of N, of P, and of T on the yield strength we set the viscoelastic limit to the reported temperatures for single and polycrystal. Then we define two reference adiabats from the upper and lower intersection of the elastic P-T paths with thes two limits (Fig. 1b) and bracket ΔP and ΔT . The validity of the adiabatic approach is confirmed though the agreement of the assessed temperatures with the temperatures obtaine from N-aggregation states (Fig. 2 and Table 1). A similar finding was reported by Anzolini et al. (2019) for single periclase inclusions from the TZ ¹⁹.

307

308

309

310

311

312

313

314

315

316

317

318

319

320

321

322

323

324

325

326

327

328

329

330

331

332

333

335	Supplemental Information
336	Supplemental Information includes three figures and four tables
337	
338	Acknowledgements
339	This work was supported through NSF-EAR 1838330, EAR-1942042. The Advanced
340	Light Source is supported through Contract No. DE-AC02-05CH11231.
341	
342	DECLARATION OF INTERESTS
343	The authors declare no competing interests.

References

- Brenker, F. E., Stachel, T. & Harris, J. W. Exhumation of lower mantle inclusions in diamond: ATEM investigation of retrograde phase transitions, reactions and exsolution. *Earth Planet. Sci. Lett.* 198, 1–9 (2002).
- Stachel, T., Harris, J. W., Brey, G. P. & Joswig, W. Kankan diamonds (Guinea)
 II: lower mantle inclusion parageneses. *Contrib. to Mineral. Petrol.* 140, 16–27 (2000).
- 3. Pearson, D. G. *et al.* Hydrous mantle transition zone indicated by ringwoodite included within diamond. *Nature* **507**, 221–224 (2014).
- Navon, O. *et al.* Solid molecular nitrogen (δ-N 2) inclusions in Juina diamonds: Exsolution at the base of the transition zone. *Earth Planet. Sci. Lett.* 464, 237–247 (2017).
- 5. Tschauner, O. *et al.* Ice-VII inclusions in diamonds: Evidence for aqueous fluid in Earth's deep mantle. *Science (80-.).* **359**, 1136–1139 (2018).
- 6. Nestola, F. *et al.* CaSiO3 perovskite in diamond indicates the recycling of oceanic crust into the lower mantle. *Nature* **555**, 237–241 (2018).
- 7. Rohrbach, A. & Schmidt, M. W. Redox freezing and melting in the Earth's deep mantle resulting from carbon–iron redox coupling. *Nature* **472**, 209–212 (2011).
- 8. Anzolini, C. *et al.* Depth of formation of CaSiO 3 -walstromite included in super-deep diamonds. *Lithos* **265**, 138–147 (2016).
- 9. Angel, R. J., Mazzucchelli, M. L., Alvaro, M., Nimis, P. & Nestola, F. Geobarometry from host-inclusion systems: The role of elastic relaxation. *Am. Mineral.* **99**, 2146–2149 (2014).
- Weidner, D. J., Wang, Y. & Vaughan, M. T. Strength of Diamond. *Science* (80-.). 266, 419–422 (1994).
- 11. Yu, X. *et al.* Constitutive Law and Flow Mechanism in Diamond Deformation. *Sci. Rep.* **2**, 876 (2012).

- Taylor, W. R., Jaques, A. L. & Ridd, M. Nitrogen-defect aggregation characteristics of some Australasian diamonds; time-temperature constraints on the source regions of pipe and alluvial diamonds. *Am. Mineral.* 75, 1290–1310 (1990).
- 13. Boyd, S. R., Kiflawi, I. & Woods, G. S. Infrared absorption by the B nitrogen aggregate in diamond. *Philos. Mag. B* **72**, 351–361 (1995).
- 14. Boyd, S. R., Kiflawi, I. & Woods, G. S. The relationship between infrared absorption and the A defect concentration in diamond. *Philos. Mag. B* **69**, 1149–1153 (1994).
- 15. Clark, C. D. & Davey, S. T. One-phonon infrared absorption in diamond. *J. Phys. C Solid State Phys.* **17**, 1127–1140 (1984).
- Chaves, M. L. S. ., Karfunkel, J., Hoppe, A. & Hoover, D. . Diamonds from the Espinhaço Range (Minas Gerais, Brazil) and their redistribution through the geologic record. *J. South Am. Earth Sci.* 14, 277–289 (2001).
- Timmerman, S., Krebs, M. Y., Pearson, D. G. & Honda, M. Diamond-forming media through time – Trace element and noble gas systematics of diamonds formed over 3 billion years of Earth's history. *Geochim. Cosmochim. Acta* 257, 266–283 (2019).
- 18. Stixrude, L. & Lithgow-Bertelloni, C. Thermodynamics of mantle minerals II. Phase equilibria. *Geophys. J. Int.* **184**, 1180–1213 (2011).
- 19. Anzolini, C. *et al.* Depth of diamond formation obtained from single periclase inclusions. *Geology* **47**, 219–222 (2019).
- 20. Rohrbach, A., Ghosh, S., Schmidt, M. W., Wijbrans, C. H. & Klemme, S. The stability of Fe–Ni carbides in the Earth's mantle: Evidence for a low Fe–Ni–C melt fraction in the deep mantle. *Earth Planet. Sci. Lett.* **388**, 211–221 (2014).
- Litasov, K. D., Shatskiy, A. & Ohtani, E. Melting and subsolidus phase relations in peridotite and eclogite systems with reduced COH fluid at 3–16
 GPa. Earth Planet. Sci. Lett. 391, 87–99 (2014).

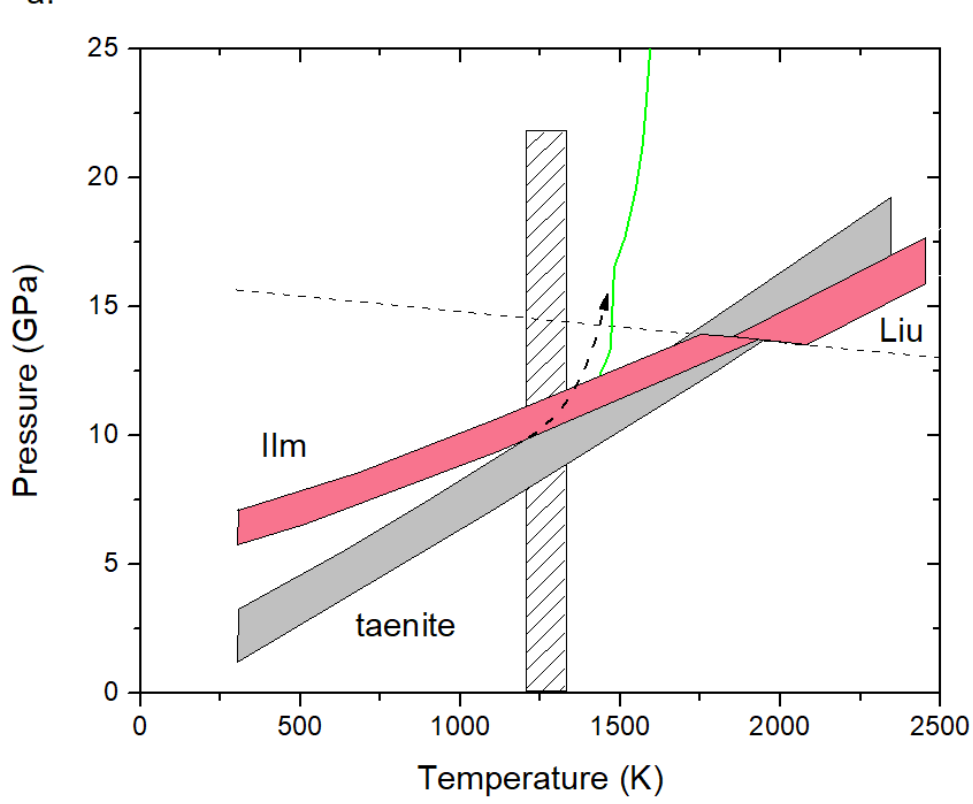
- 22. Ghosh, S., Ohtani, E., Litasov, K. D. & Terasaki, H. Solidus of carbonated peridotite from 10 to 20 GPa and origin of magnesiocarbonatite melt in the Earth's deep mantle. *Chem. Geol.* **262**, 17–28 (2009).
- 23. Nishi, M. *et al.* Stability of hydrous silicate at high pressures and water transport to the deep lower mantle. *Nat. Geosci.* 7, 224–227 (2014).
- 24. Palot, M. *et al.* Evidence for H2O-bearing fluids in the lower mantle from diamond inclusion. *Lithos* **265**, 237–243 (2016).
- 25. Huang, S. *et al.* HIMU geochemical signature originating from the transition zone. *Earth Planet. Sci. Lett.* **542**, 116323 (2020).
- 26. Smith, E. M. *et al.* Large gem diamonds from metallic liquid in Earth's deep mantle. *Science* (80-.). **354**, 1403–1405 (2016).
- 27. Giannozzi, P. *et al.* QUANTUM ESPRESSO: a modular and open-source software project for quantum simulations of materials. *J. Phys. Condens. Matter* **21**, 395502 (2009).
- Hålenius, U., Hatert, F., Pasero, M. & Mills, S. J. New minerals and nomenclature modifications approved in 2018. *Mineral. Mag.* 82, 1369–1379 (2018).
- 29. Kresse, G. & Furthmüller, J. Efficient iterative schemes for ab initio totalenergy calculations using a plane-wave basis set. *Phys. Rev. B* **54**, 11169– 11186 (1996).
- 30. Togo, A. & Tanaka, I. First principles phonon calculations in materials science. *Scr. Mater.* **108**, 1–5 (2015).
- 31. Dorogokupets, P. I., Dymshits, A. M., Litasov, K. D. & Sokolova, T. S. Thermodynamics and Equations of State of Iron to 350 GPa and 6000 K. *Sci. Rep.* **7**, 41863 (2017).
- 32. Troullier, N. & Martins, J. L. Efficient pseudopotentials for plane-wave calculations. II. Operators for fast iterative diagonalization. *Phys. Rev. B* **43**, 8861–8869 (1991).

- 33. Vanderbilt, D. Soft self-consistent pseudopotentials in a generalized eigenvalue formalism. *Phys. Rev. B* **41**, 7892–7895 (1990).
- 34. Anisimov, V. I., Zaanen, J. & Andersen, O. K. Band theory and Mott insulators: Hubbard U instead of Stoner I. *Phys. Rev. B* **44**, 943–954 (1991).
- 35. Cococcioni, M. & de Gironcoli, S. Linear response approach to the calculation of the effective interaction parameters in the LDA+U method. *Phys. Rev. B* **71**, 035105 (2005).
- 36. Shukla, G. *et al.* Thermoelasticity of Fe 2+ -bearing bridgmanite. *Geophys. Res. Lett.* **42**, 1741–1749 (2015).
- 37. Hamann, D. R. H2O hydrogen bonding in density-functional theory. *Phys. Rev. B* **55**, R10157–R10160 (1997).
- 38. Perdew, J. P., Burke, K. & Ernzerhof, M. Generalized Gradient Approximation Made Simple. *Phys. Rev. Lett.* **77**, 3865–3868 (1996).
- 39. Hemley, R. J. *et al.* Static compression of H2O-ice to 128 GPa (1.28 Mbar). *Nature* **330**, 737–740 (1987).
- 40. Somayazulu, M. *et al.* In situ high-pressure x-ray diffraction study of H2 O ice VII. *J. Chem. Phys.* **128**, (2008).
- 41. Munro, R. G., Block, S., Mauer, F. A. & Piermarini, G. Isothermal equations of state for H2O-VII and D2O-VII. *J. Appl. Phys.* **53**, 6174–6178 (1982).
- 42. Wolanin, E. et al. Equation of state of ice VII up to 106 GPa. Phys. Rev. B Condens. Matter Mater. Phys. **56**, 5781–5785 (1997).
- 43. Loubeyre, P., LeToullec, R., Wolanin, E., Hanfland, M. & Hausermann, D. Modulated phases and proton centring in ice observed by X-ray diffraction up to 170 GPa. *Nature* **397**, 503–506 (1999).
- 44. Sugimura, E. *et al.* Experimental evidence of superionic conduction in H2O ice. *J. Chem. Phys.* **137**, (2012).
- 45. Fortes, A. D., Wood, I. G., Tucker, M. G. & Marshall, W. G. The P-V-T equation of state of D2O ice VI determined by neutron powder diffraction in

- the range 0 < P < 2.6 GPa and 120 < T < 330 K, and the isothermal equation of state of D2O ice VII from 2 to 7 GPa at room temperature. *J. Appl. Crystallogr.* **45**, 523–534 (2012).
- 46. Klotz, S. *et al.* Bulk moduli and equations of state of ice VII and ice VIII. *Phys. Rev. B* **95**, 1–7 (2017).
- 47. Sugimura, E. *et al.* Compression of H2 O ice to 126 GPa and implications for hydrogen-bond symmetrization: Synchrotron x-ray diffraction measurements and density-functional calculations. *Phys. Rev. B Condens. Matter Mater. Phys.* 77, 1–6 (2008).
- 48. Bezacier, L. *et al.* Equations of state of ice VI and ice VII at high pressure and high temperature. *J. Chem. Phys.* **141**, (2014).
- 49. Sanchez-Valle, C., Mantegazzi, D., Bass, J. D. & Reusser, E. Equation of state, refractive index and polarizability of compressed water to 7 GPa and 673 K. *J. Chem. Phys.* **138**, (2013).
- 50. Abramson, E. H. & Brown, J. M. Equation of state of water based on speeds of sound measured in the diamond-anvil cell. *Geochim. Cosmochim. Acta* **68**, 1827–1835 (2004).
- 51. Asahara, Y., Murakami, M., Ohishi, Y., Hirao, N. & Hirose, K. Sound velocity measurement in liquid water up to 25 GPa and 900 K: Implications for densities of water at lower mantle conditions. *Earth Planet. Sci. Lett.* **289**, 479–485 (2010).
- 52. Tronche, E. J. *et al.* The thermal equation of state of FeTiO3 ilmenite based on in situ X-ray diffraction at high pressures and temperatures. *Am. Mineral.* **95**, 1708–1716 (2010).
- 53. Wechsler, B. A. & Prewitt, C. T. Crystal structure of ilmenite (FeTiO3) at high temperature and at high pressure. *Am. Mineral.* **69**, 176–185 (1984).

- 54. Yamanaka, T., Komatsu, Y. & Nomori, H. Electron density distribution of FeTiO3 ilmenite under high pressure analyzed by MEM using single crystal diffraction intensities. *Phys. Chem. Miner.* **34**, 307–318 (2007).
- Yamanaka, T., Komatsu, Y., Sugahara, M. & Nagai, T. Structure change of MgSiO3, MgGeO3, and MgTiO3 ilmenites under compression. *Am. Mineral.* 90, 1301–1307 (2005).
- 56. Ming, L. C., Kim, Y.-H., Uchida, T., Wang, Y. & Rivers, M. In situ X-ray diffraction study of phase transitions of FeTiO 3 at high pressures and temperatures using a large-volume press and synchrotron radiation. *Am. Mineral.* **91**, 120–126 (2006).
- 57. Leinenweber, K., Utsumi, W., Tsuchida, Y., Yagi, T. & Kurita, K. Unquenchable high-pressure perovskite polymorphs of MnSnO3 and FeTiO3. *Phys. Chem. Miner.* **18**, 244–250 (1991).
- 58. Wang, W., Zhang, H., Brodholt, J. P. & Wu, Z. Elasticity of hydrous ringwoodite at mantle conditions: Implication for water distribution in the lowermost mantle transition zone. *Earth Planet. Sci. Lett.* **1**, 116626 (2020).





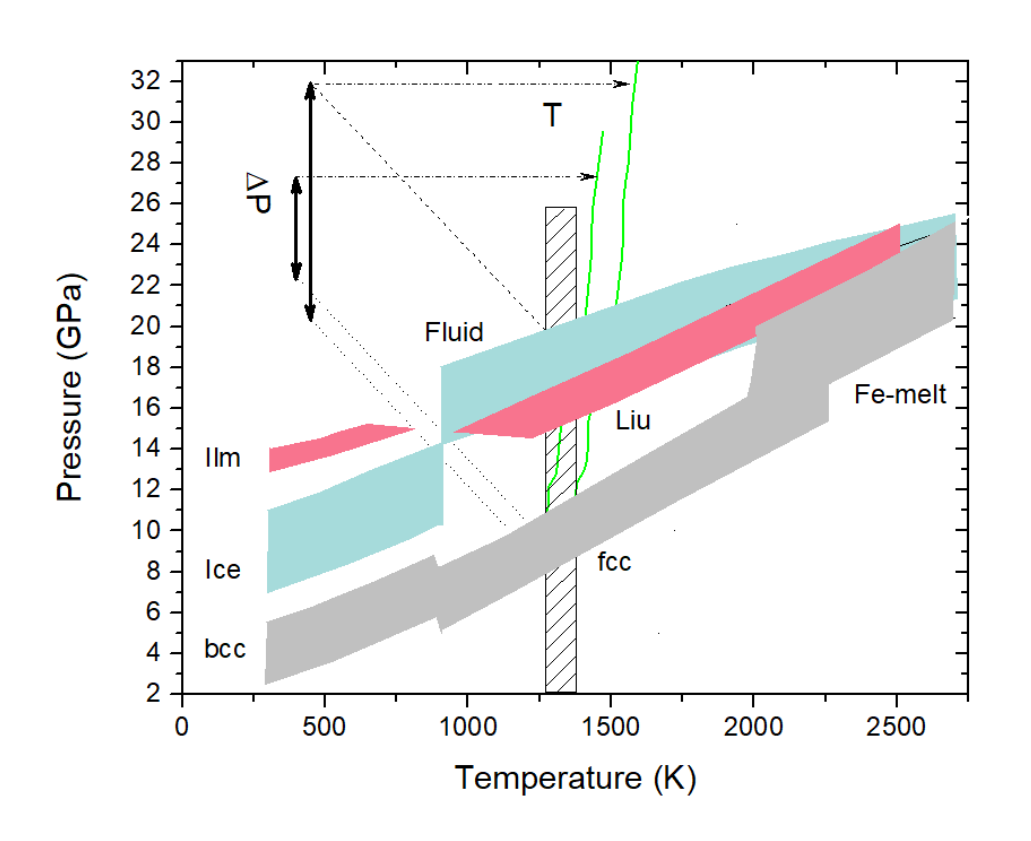


Figure 1. P-T paths of high-pressure inclusions in diamonds. a: Inclusions of ilmenite (ilm>95, geik<5, red) and taenite (Fe50Ni50, grey) observed in a diamond from the Diamantina alluvial deposits (Methods). The calculated elastic release paths start to intersect at the diamond viscoelastic limit (hashured area). This indicates that the inclusions were in elastic equilibrium with the surrounding diamond above this limit. Above this limit P-T is expected to have evolved close to a mantle adiabat (green line). The ilmenite-liuite phase boundary is indicated. b: Inclusions of ilmenite (ilm92geik7, red) and iron (Fe>95, Ni, grey) in a diamond from Orapa, Botswana. The range of foot pressures and P-T paths reflect the uncertainties (see Methods). Offsets of paths are result of phase transformations. Grey hashured region indicates the transition from elastic to viscoelastic deformation of diamond. We assess the corresponding T through intersection of a reference adiabat (green) with $P+\Delta P$ (indicated through dashed lines). This $P + \Delta P$ and T gives a lower limit of P-T of entrapment. However, the temperature of this lower limit matches the temperature estimate from nitrogen defect distribution in this diamond (table 1). This shows that the lower limit represents the actual P-T path quite closely.

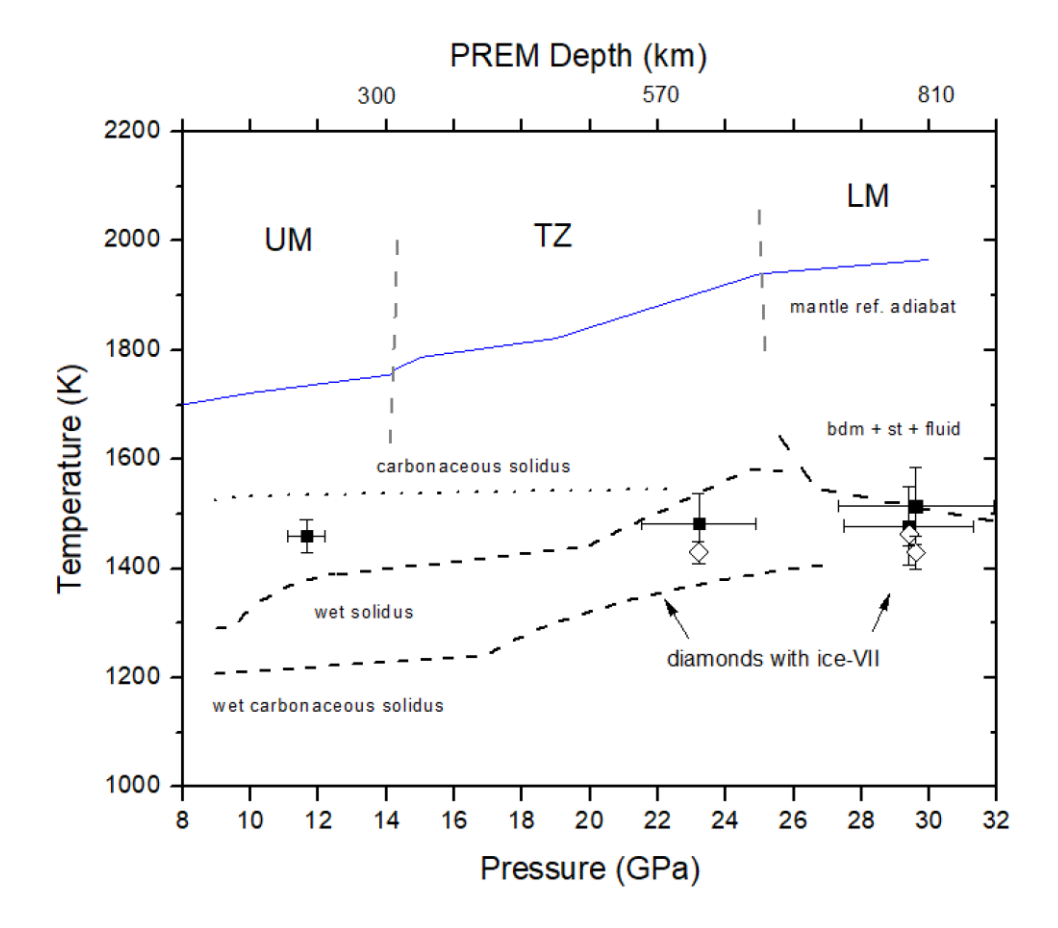


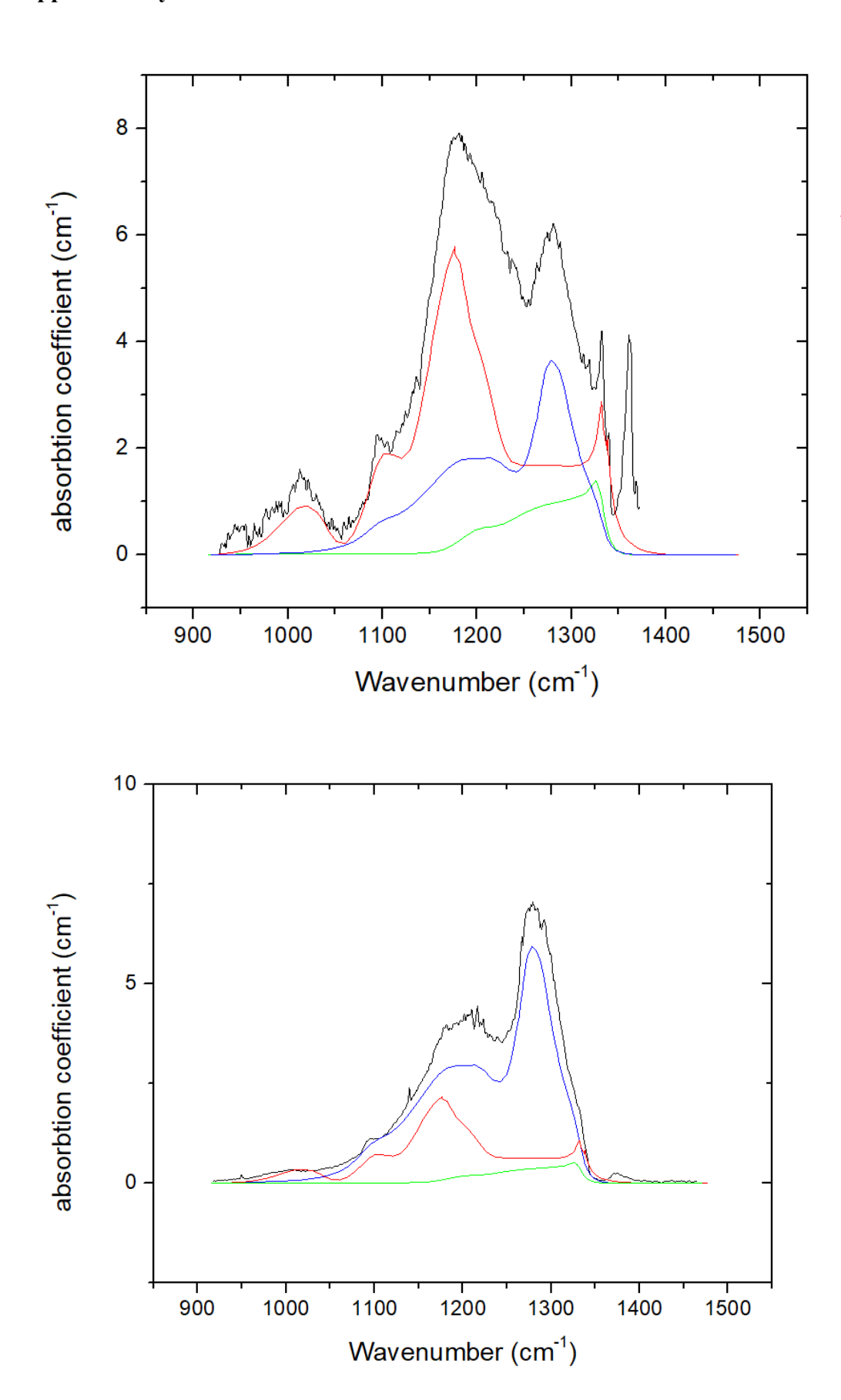
Figure 2. P-T points of entrapment of inclusions in diamonds. Black squares, assessment based on adiabatic approach; hollow diamonds, temperature assessed through nitrogen aggregation. Reference mantle adiabat is from 18 , carbonaceous, wet, and wet-carbonaceous solidus of peridotite are from 5,21,22 . The decomposition boundary of phase D to bridgmanite (bdm), stishovite (st), and fluid was taken from 23 . All inclusions were entrapped in diamonds which grew in cool wet environments down to 820 km depth. Consistent with experiments, these diamonds grew above the solidus of C-H-O fluid bearing peridotite 21 . Diamond formation is tied to local wet areas in the TZ 58 and dehydration of phases B and D 23 above ~ 800 km.

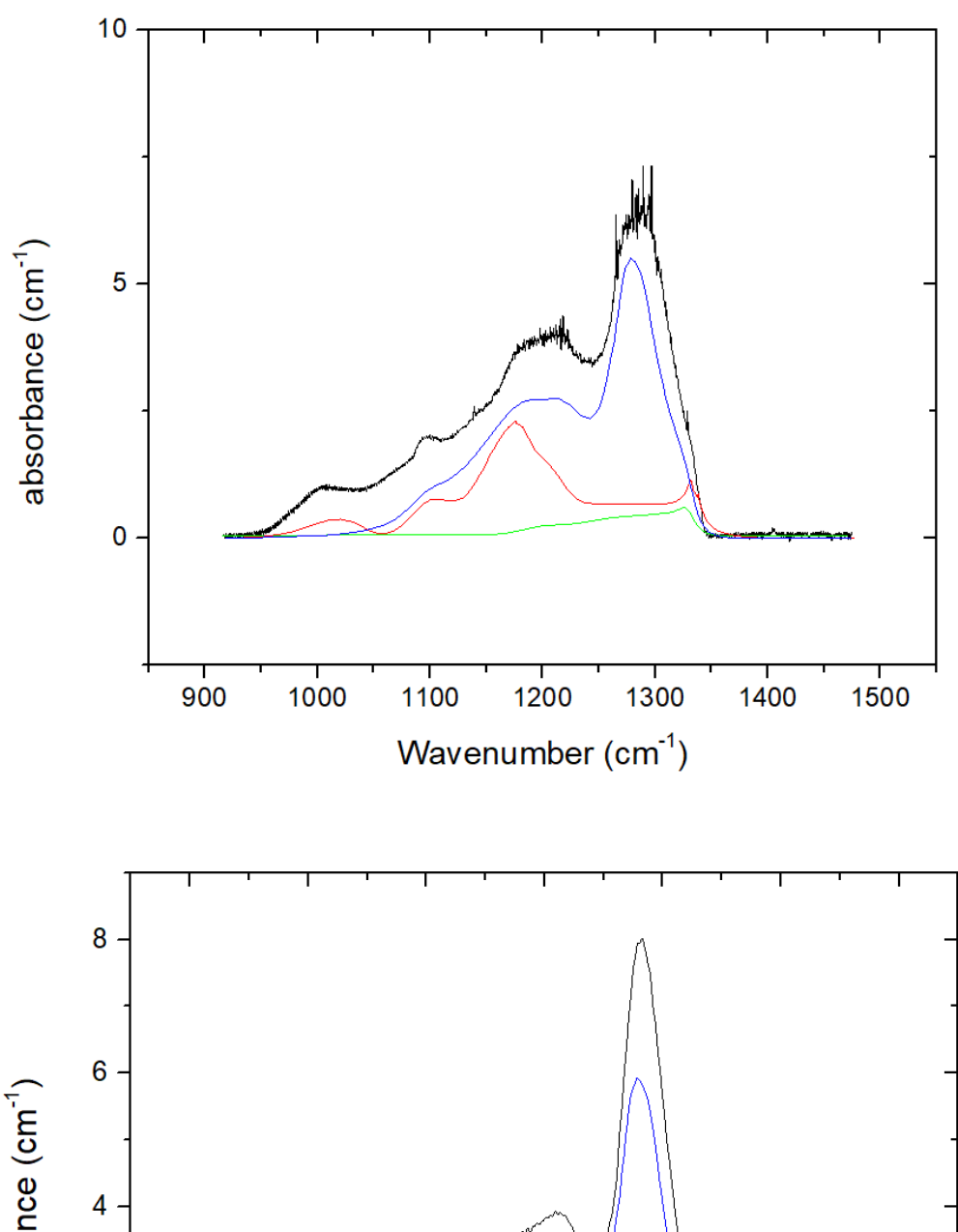
Table 1. Pressures and temperatures from the adiabatic approach compared to temperatures from nitrogen aggregation ¹² using ages from ^{16,17}. Further details are given in Methods.

Specimen		Nitrogen A	Adiabatic P-T			
Specimen	A (ppm)	B (ppm)	Age (Ga)	T (K)	T (K)	P (GPa)
Orapa GRr1507	94±9	49±7	0.9 -1.6	1430±30	1420±20	28.6±1.4
Orapa GRr1519	87±9	53±7	0.9-1.6	1430±20	1490±50	23.3±2.0
Orapa M57666	96±6	68±7	0.9-1.6	1460±20	1442±40	29.0±2.0
Diamantina	52±12	134±15	>1.7	1460±30	-	11.6±0.6*

^{*}From elastic P-T paths and temperature from N aggregation.

Supplementary materials





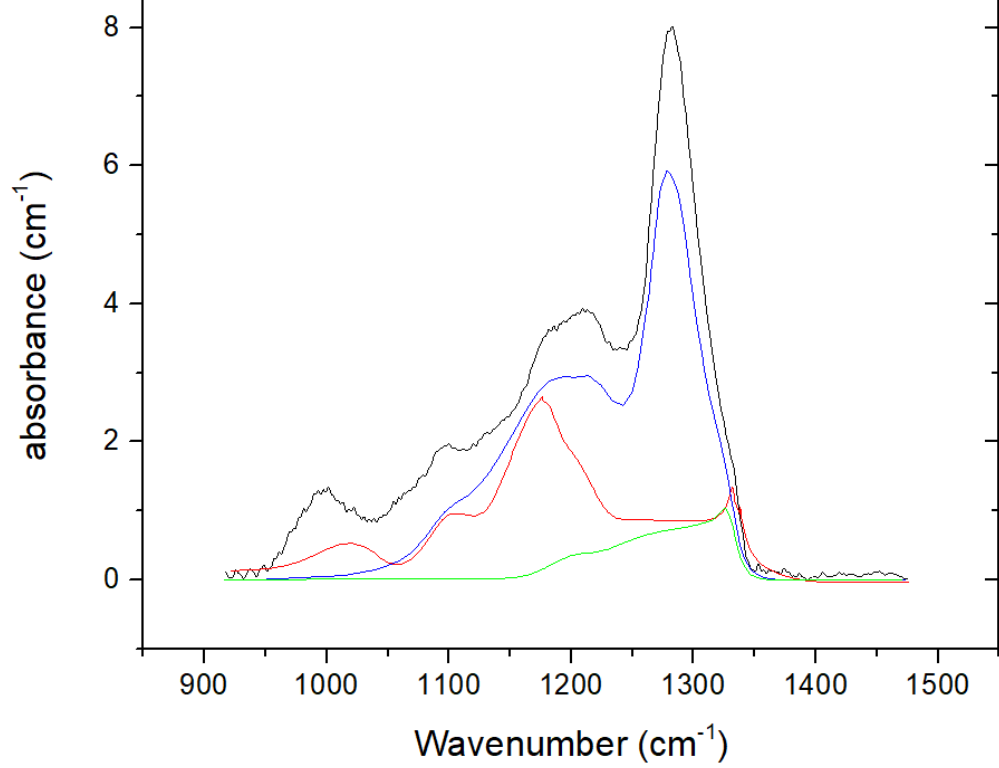


Figure S1. Infrared spectra in the energy range of N-defect absorption bands. The spectra were normalized relative to a type-II standard at the energy of 1272 cm⁻¹. Background was fitted and subtracted. Black, observed data; blue, A-type defects; red, B-type defects; green, D-type defects (all defect spectra are taken from Taylor et al. (1990) ¹²). From the top to the bottom figures are Diamantina, GRR1507, GRr1519, GRR1521, respectively.

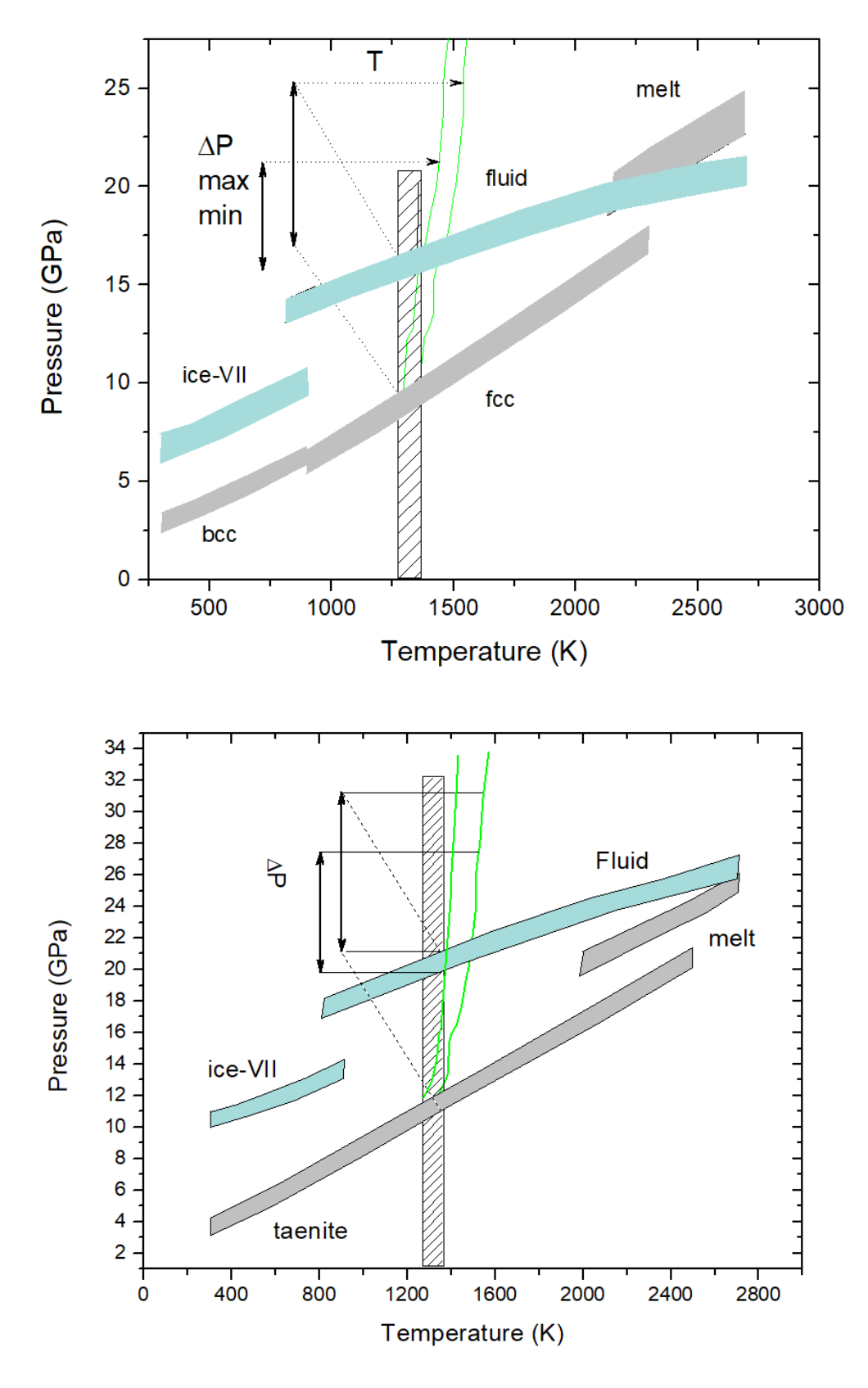


Figure S2. Calculated elastic P-T paths and assessment of adiabatic P-T conditions for GRr1507 (a), GRr1519 (b), and M57666 (c).

Table S1. The elastic P-T paths for GRr1519.

Temperature (K)	Pressure (GPa)					
Phase	bcc-iron	fcc-iron	Iron melt	Ice-VII	fluid	
300	2.4-3.4	-	-	6.0-7.4	-	
500	3.4-4.4	-	-	7.0-8.4	-	
700	4.6-5.6	-	-	8.2-9.6	-	
900	5.9-6.8	5.4-7.3	-	9.3-10.8	13.6-14.8	
1100	-	6.9-8.8	-	-	14.5-15.8	
1300	-	8.5-10.4	-	-	15.4-16.7	
1500	-	10.1-12.0	-	-	16.3-17.6	
1800		12.5-14.4	-	-	17.6-18.9	
2000	-	14.1-16.0	18.5-20.5	-	18.3-19.7	
2300	-	16.6-18.6	19.8-22.0	-	19.3-20.7	
2500	-	-	21.2-23.4	-	19.7-21.2	
2700		-	22.7-24.9	-	20.1-21.6	

Table S2. The elastic P-T paths for GRr1507

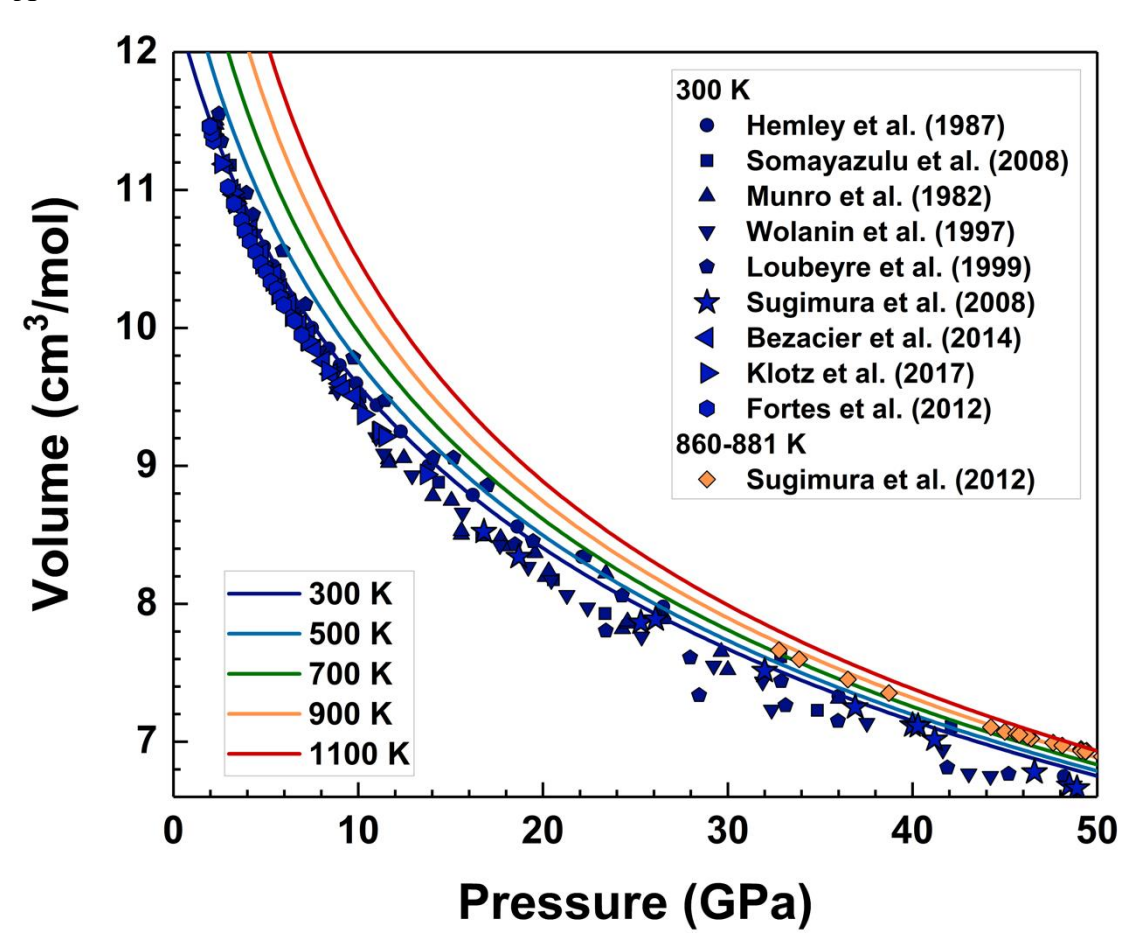
Town and time (I/)			D-	oggung (CDs	`		
Temperature (K)	Pressure (GPa)						
Phase	bcc-iron	fcc-iron	Iron melt	ilmenite	liuite	Ice-VII	Fluid H ₂ O
300	2.5-5.5	-	-	12.9-14.0	-	7.0-11.0	-
500	3.5-6.5	-	-	13.6-14.6	-	7.6-12.0	-
700	4.7-7.7	-	-	14.5-15.5	-	8.7-13.2	-
900	5.9-8.9	5.0-8.1	-	15.4-16.5	-	9.9-14.3	13.8-18.1
1100	-	6.6-9.6	-	16.1-17.7	13.7-15.8	-	14.8-19.1
1300	-	8.1-11.2	-	17.1-18.8	15.0-17.0	-	15.8-20.1
1500	-	9.7-12.8	-	-	16.2-18.3	-	16.7-21.1
1800		12.0-15.1	-	-	18.2-20.3		18.0-22.5
2000	-	13.2-16.8	15.3-20.9	-	19.5-21.6	-	18.9-23.3
2300	-	15.8-19.1	17.5-23.0	-	21.5-23.6		19.9-24.4
2500	-	-	18.9-24.5	-	22.8-24.9		20.5-25.0
2700		-	20.4-26.0	-	24.1-26.2		21.1-25.7

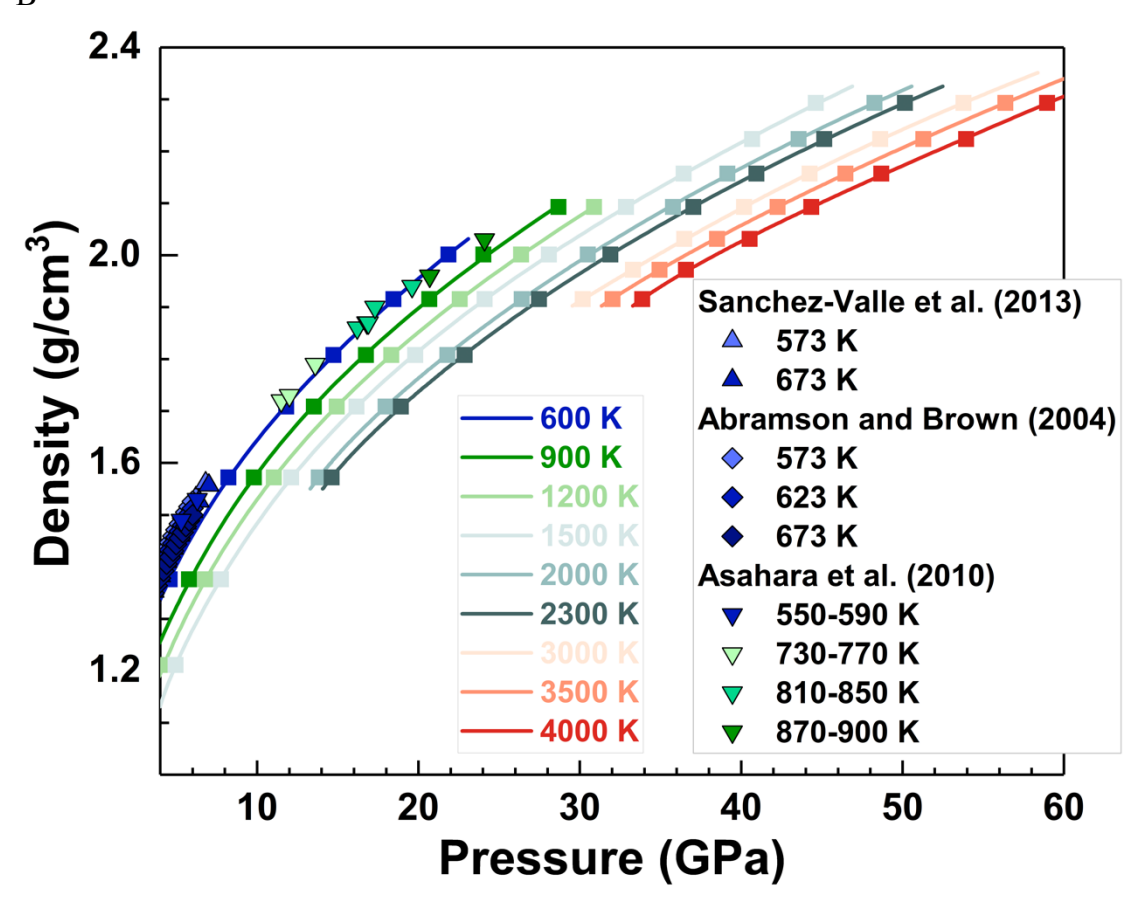
Table S3. The elastic P-T paths for M57666.

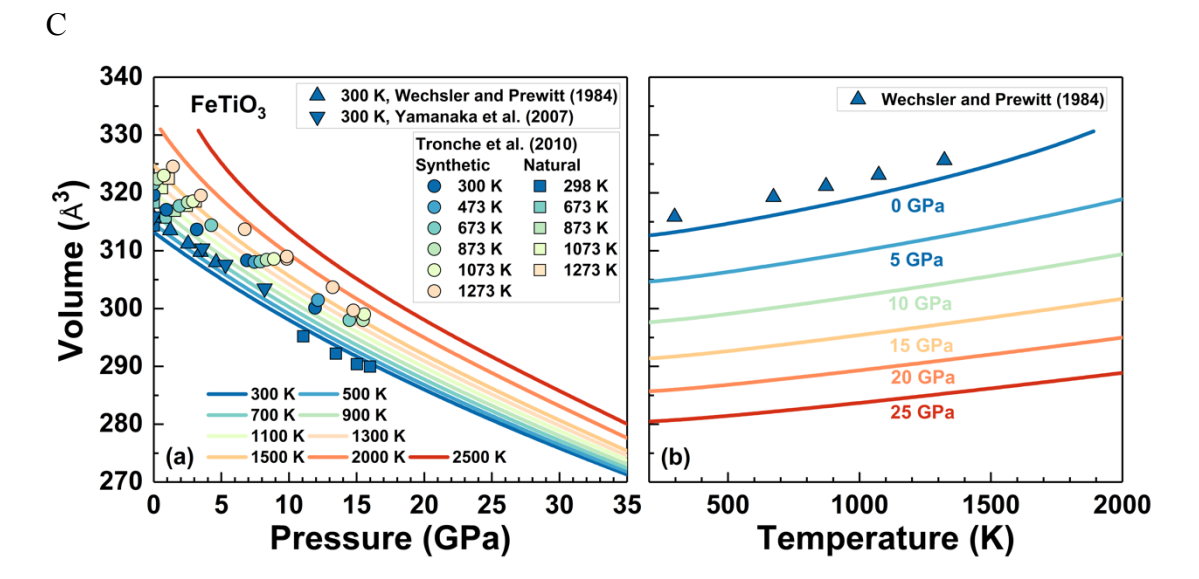
Temperature (K)	Pressure (GPa)			
Phase	fcc-iron	Iron melt	Ice-VII	Fluid H ₂ O
300	2.5-4.6	-	10.0-11.0	-
500	3.8-6.0	-	10.8-11.8	
700	5.3-7.4	-	11.8-12.9	
900	6.8-8.9	-	13.1-14.2	17.4-18.6
1100	8.5-10.7			18.6-19.8
1300	10.1-12.3			19.6-20.9
1500	11.5-13.7			20.7-22.0
1800	13.9-16.1	17.6-20.0		22.1-23.4
2000	15.5-17.8	19.0-21.4		23.1-24.4
2300	18.0-20.3	21.2-23.6		24.3-25.6
2500	19.6-21.9	22.6-25.0		25.0-26.3
2700	21.1-23.5	24.2-26.5		25.9-27.2
3000	23.8-26.2	26.4-28.8		27.1-28.4

Table S4. The elastic P-T paths for Diamantina.

Temperature (K)	Pressure (GPa)				
Phase	fcc-iron	Ilmenite	Liuite		
300	1.2-3.2	5.8-7.1	-		
500	2.5-4.6	6.5-7.8	-		
700	4.0-6.0	7.4-8.6	-		
900	5.5-7.5	8.4-9.6	-		
1100	7.1-9.2	9.3-10.6	-		
1300	8.7-10.8	10.4-11.6	-		
1500	10.1-12.2	11.4-12.6	-		
1800	12.5-14.7	13.0-14.2	11.7-13.4		
2000	14.1-16.3	14.0-15.3	12.9-14.7		







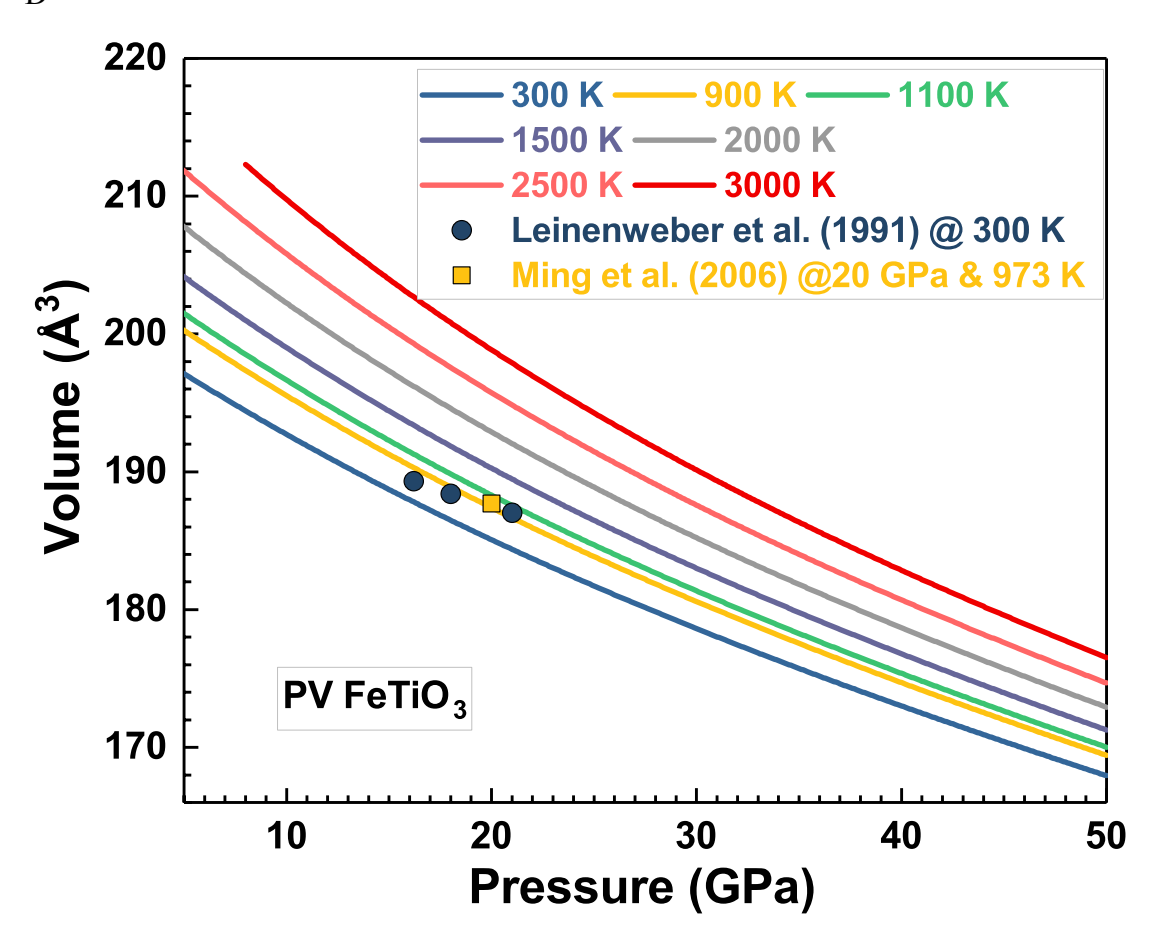
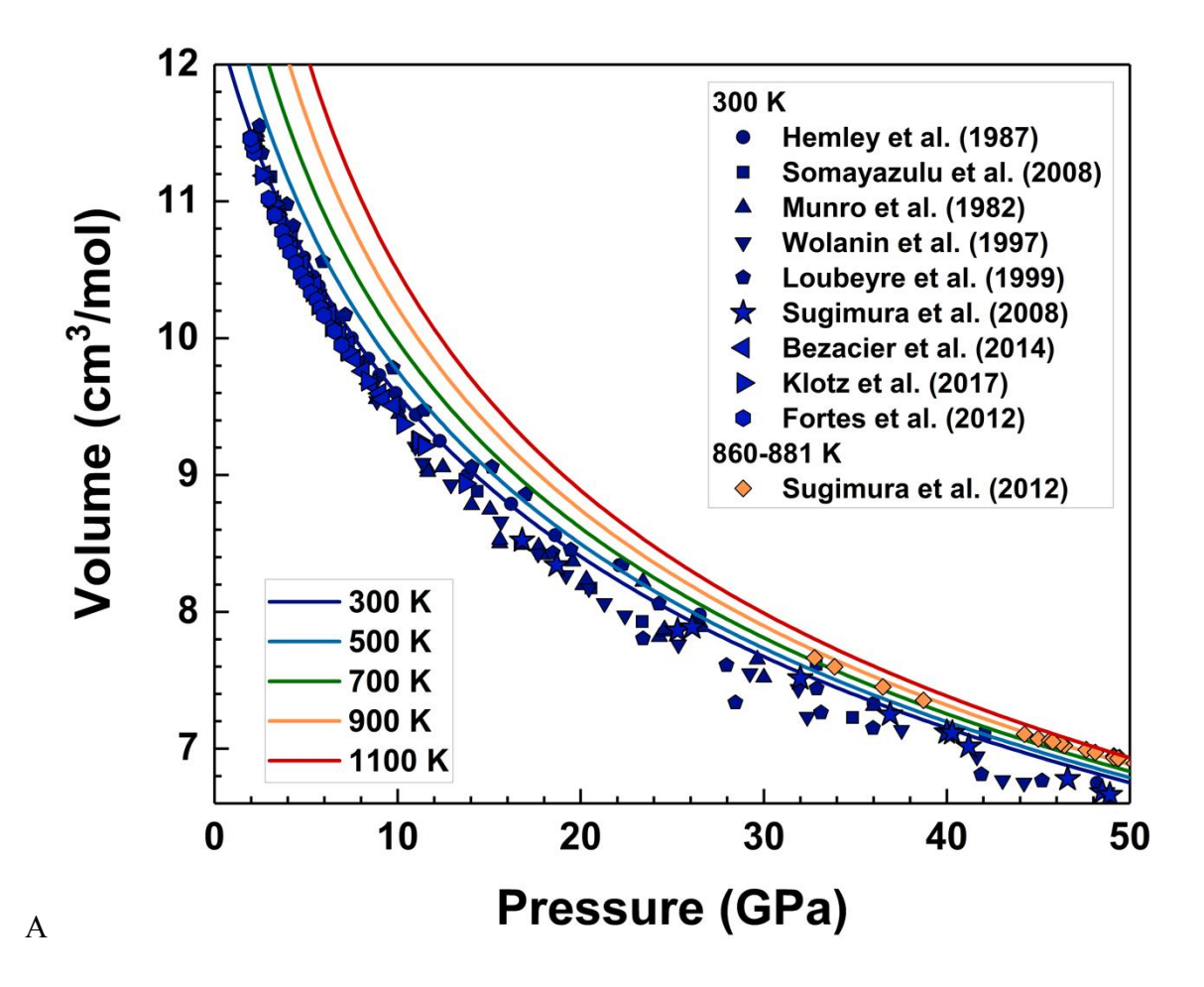
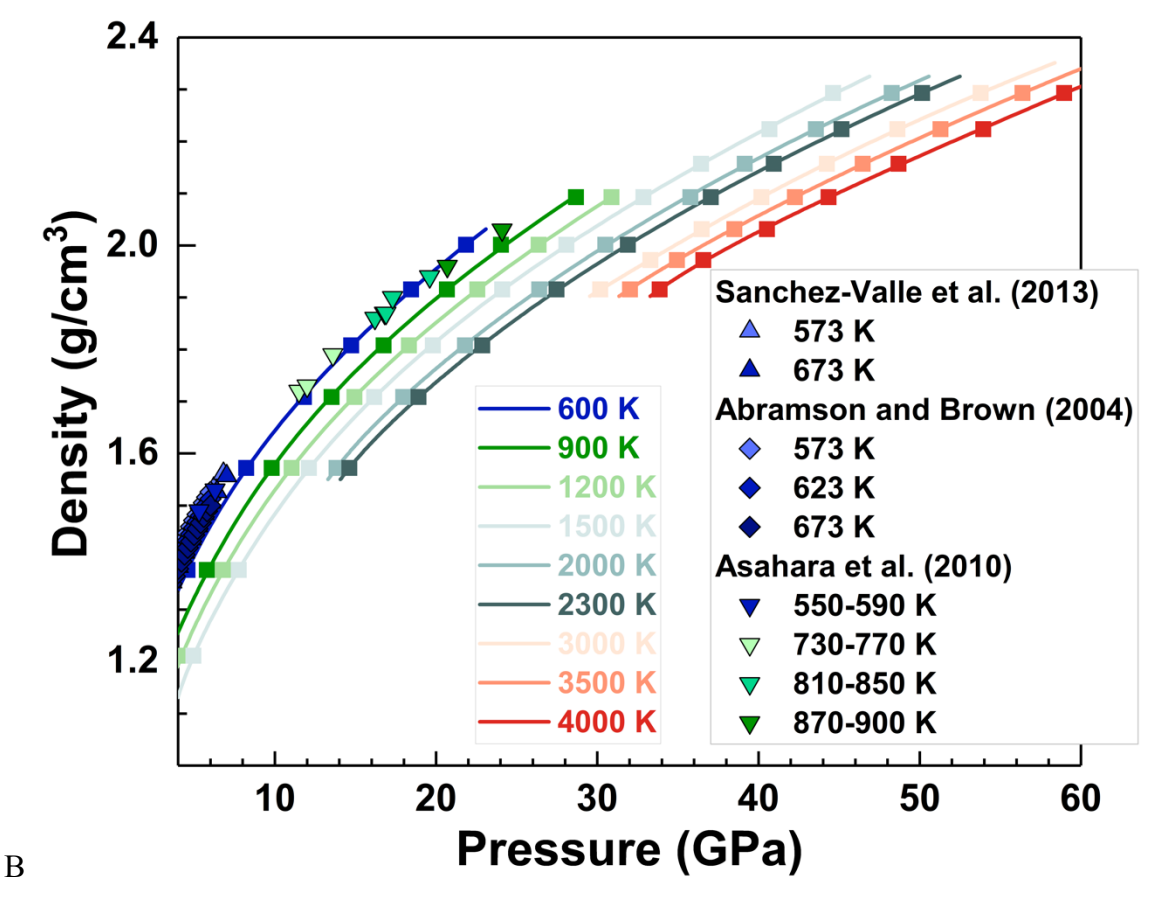
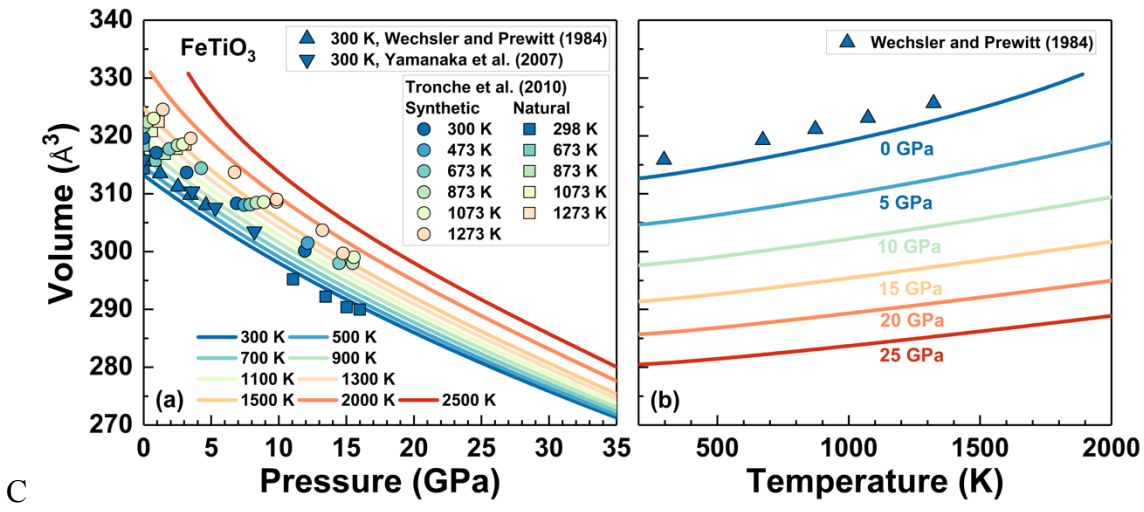


Figure S3. The calculated equation of states of ice-VII, H₂O fluid, FeTiO₃ ilmenite, and liuite (PV FeTiO₃) compared with experimental data. A, ice-VII, colored lines represent the calculated results from this study at different temperatures, and scatters are experimental measurements from previous studies (38-46). B, H₂O fluid, triangles and rhombuses are experimental data (47-49), and the lines marked by squares are our calculated results. C, FeTiO₃ ilmenite, scatters represent experimental measurements from previous studies (50-52), and colored lines are the calculated results. D, liuite (Perovskite (PV) FeTiO₃), squares and circles are experimental data from Ming et al. (2006) (53) and Leinenweber et al. (1991) (54), respectively.







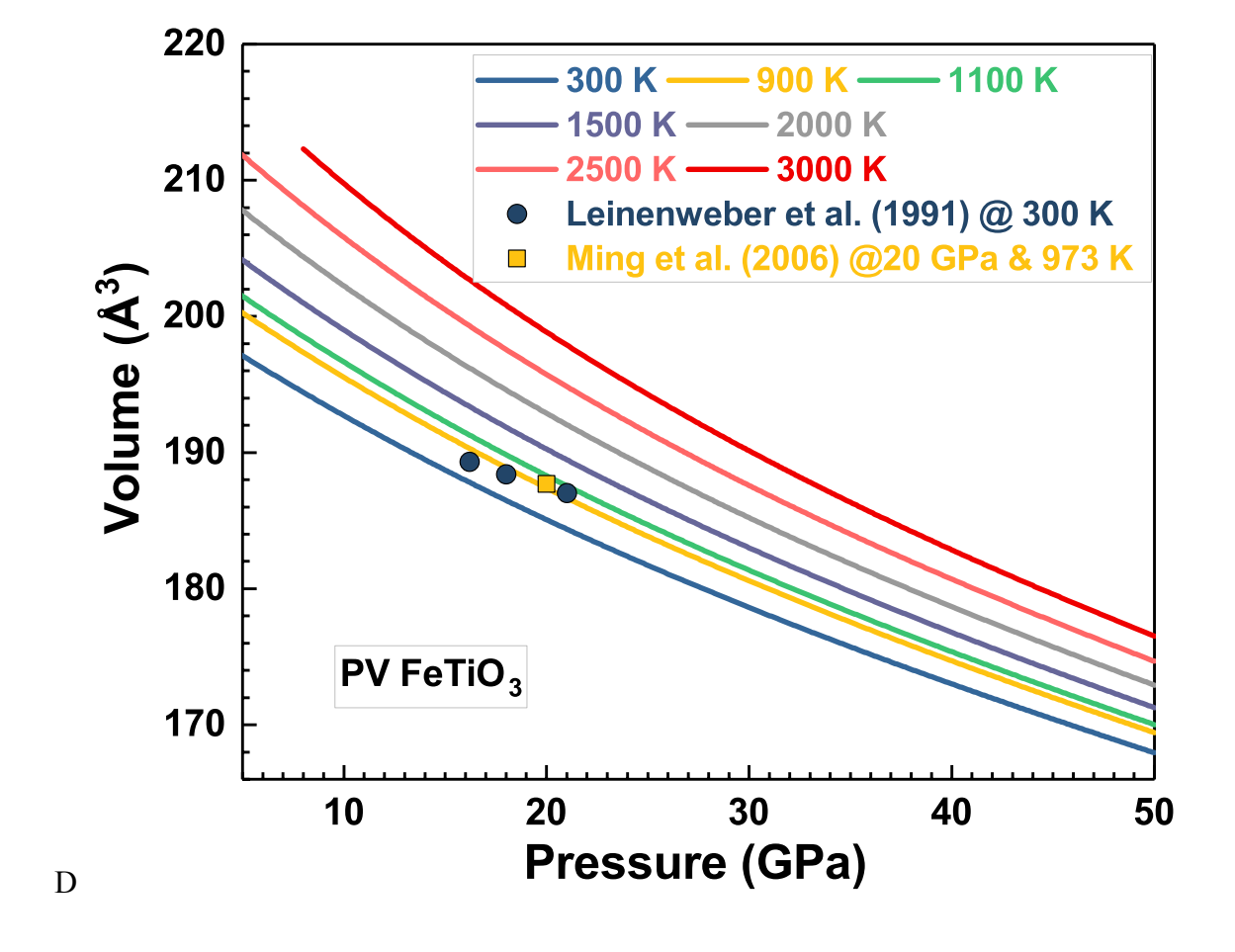


Figure S3. The calculated equation of states of ice-VII, H₂O fluid, FeTiO₃ ilmenite, and liuite (PV FeTiO₃) compared with experimental data. A, ice-VII, colored lines represent the calculated results from this study at different temperatures, and scatters are experimental measurements from previous studies ^{39–43,45–48}. B, H₂O fluid, triangles and rhombuses are experimental data ^{49–51}, and the lines marked by squares are our calculated results. C, FeTiO₃ ilmenite, scatters represent experimental measurements from previous studies ^{52–54}, and colored lines are the calculated results. D, liuite (Perovskite (PV) FeTiO₃), squares and circles are experimental data from Ming et al. (2006) ⁵⁶ and Leinenweber et al. (1991) ⁵⁷, respectively.